Islam *et al.*
Journal of Engineering and Applied Science (2024) 71:134
https://doi.org/10.1186/s44147-024-00465-z

Journal of Engineering and Applied Science

RESEARCH Open Access

Nano-structured metamaterial absorber based on a plus-shaped resonator for optical wavelength applications

Istiaq Mohammad Tanvirul Islam[1*], Sikder Sunbeam Islam[1], Md. Rashedul Islam[2], Abu Naser Md. Rezaul Karim[2] and Rezaul Azim[3]

*Correspondence: strangrtanvir@gmail.com

[1] Department of Electrical and Electronic Engineering, International Islamic University Chittagong, Chittagong, Bangladesh
[2] Department of Computer Science and Engineering, International Islamic University Chittagong, Chittagong, Bangladesh
[3] Department of Physics, Chittagong University, Chittagong, Bangladesh

Abstract

Metamaterial absorbers have sparked widespread interest due to their remarkable electromagnetic properties, which enable a wide range of applications in light absorption and manipulation. This study introduces a new three-layer nanomaterial absorber (NMA) unit cell composed of nickel (Ni), silicon dioxide (SiO_2), and nickel (Ni) designed to operate across the entire visible spectrum (390–780 nm). We demonstrate the NMA's exceptional absorption characteristics through rigorous numerical simulations using industry-standard software, achieving a mean absorption rate of 97.17% and a maximum absorption peak of 99.99% at 694.89 nm under standard angles. Furthermore, the NMA unit cell has good impedance matching, efficient coupling between capacitors and inductors, and significant plasmonic resonance properties. Fabrication feasibility and potential applications in solar energy harvesting, optical sensing, and light detection.

Keywords: Wide-band, Metamaterial absorber, Polarization-independent, Impedance match, Optical regions

Introduction

Metamaterials (MM) have attracted the interest of the scientific community in recent decades, owing to their dual properties of negative electric permittivity and magnetic permeability [1]. Because of their unique and unusual features, metamaterials (MM) have attracted a lot of interest in both the scientific and technical fields from its theoretical inception by V.G. Veselago in 1968 [2]. Rodger M. Walser examined the term "metamaterials" to designate artificially created composite materials distinguished by a periodic unit structure [3]. It is important to remember that metamaterials, also known as MM, are clearly man-made materials that were purposefully created and do not exist naturally in the environment [4, 5]. In this context, a metamaterial absorber (MMA) functions as a customized device created to absorb incident electromagnetic radiation at its chosen operating frequency [6]. Landy successfully showed the first metamaterial absorber's (MMA) capability inside the microwave frequency range. This accomplishment resulted in an absorption efficiency of 88% and was made possible by

the independent modification of the metamaterials' effective magnetic permeability and effective electric permittivity [7]. After Landy's first introduction of the narrowband, single-frequency absorber, other researchers have worked to improve broadband absorption technology. The effectiveness of absorption has significantly increased as a result of this group effort [8–10]. Numerous engineering applications have used metamaterials; this includes applications in areas such as antennas [11, 12], invisibility cloaks [13], optical imaging [14], absorption devices [15], filters [16], highly sensitive sensors [17], and photovoltaic cells [18]. While metamaterial absorbers (MMA) provide a number of advantages, it is important to note that once an absorber's structural structure is identified, perfect absorption can only occur at a particular, predetermined frequency. This limitation may limit the device's adaptability in real-world applications [19, 20]. In-depth research is also being done on metamaterials for a variety of applications including perfect absorbers across millimeter to nanometer wavelengths [7], flexible metamaterials [21], multiband metamaterials [22], polarization-insensitive absorbers [23], broadband absorbers [24], and single-band absorbers [7], multiband absorber [25], and detectors [26], polarization-insensitive [27, 28] to polarization-sensitive [29] and sensors [30]. Tao et al. introduced a metamaterial absorber designed for terahertz frequency utilization, employing both numerical modeling and experimental research. Their unit cell structure comprises two metallic layers, an electric ring resonator, and a cut wire, responsible for generating electric and magnetic responses. Through numerical simulations, their study demonstrated an absorption efficiency of 98% at 1.12 THz. Experimental validation further confirmed a 70% absorption rate at 1.3 THz [31]. Zhang et al. obtained more than 95% infrared absorption by sketching a dual-band metamaterial absorber with a five-layered metal–insulator-metal [32]. Their absorber structure incorporates excellent flexibility and accommodates a wide angle of incidence. Some studies have indicated that plasmonic absorbers employing rotationally symmetric structures have demonstrated the potential to achieve a peak absorption rate of up to 99%, retaining their insensitivity to applied polarization. The introduction as well as fabrication of an ultra-wideband metamaterial absorber with a wavelength range of 400 to 700 nm demonstrates a typical absorption efficiency of 92% and constructed using a Ni–Ni combined [33]. Additionally, a perfect based on tungsten-based (W) and the metal nickel (Ni) metamaterial absorber achieve a mean absorption of 90.98% spanning from 430 to 770 nm, accompanied by a 99.42% near-unity absorption peak at 579.26 THz. It also exhibits angular stability up to 45° [34]. Metamaterial absorbers tailored for solar energy applications, utilizing a structure composed of W, rexolite, and Ni in a metal–insulator-metal (MIM) configuration, achieve a standard absorption rate of over 80% within the range of 478–697 nm [35]. Furthermore, a W and SiO_2-based perfect metamaterial absorber showcases an average absorption of 97%, with a peak absorption reaching 99.99% at the wavelength of 521.83 nm [36]. A Si-based metamaterial absorber has been developed, exhibiting 98.2% maximum absorption in the visible light spectrum and 80% mean absorption within the range of 437.9–578.3 nm [37]. Gold-based NMAs exhibited a mean absorption of 90% for each of the polarizations transverse electric (TE) as well as transverse magnetic (TM) have been developed, employing for numerical analysis and an algorithm based on genetics was employed. Additionally, these absorbers demonstrate beyond 40° of polarization sensitivity [38]. Furthermore, meta-surface-based broadband solar absorbers,

composed of gold and SiO_2, exhibit a mean absorption rate of 80.24% and a peck absorption of 96.40% [39].

Based on the related works, this article presents a nearly ideal metamaterial absorber that stands out for its resistance to mechanical stress. The components of the symmetrically balanced layout are durable materials that can tolerate rising temperatures, like SiO_2 and Ni. In the visible wavelength range, it achieves a mean absorption of 97.17%, and in the UV to infrared (NIR) region, it achieves an average absorption of 96.27%. Particularly, it maintains absorption values above 99% from 579 to 780 nm and hits near-unity absorption of 99.99% at 694.89 nm. Furthermore, considering its excellent suitability for demands that involve solar energy gathering, and its mechanical resistance to stress.

Materials, method, and design of the structure

Methods

In this configuration, the central layer employs as a dielectric, silicon dioxide (SiO_2) is used substrate [40], while nickel (Ni) [41] serves as both the patch material and ground layer on both sides of the SiO_2 substrate. The basic reason for choosing nickel for both ground and the upper layer is due to its superior absorption efficiency in the visible spectrum and its suitability for high-temperature applications [41]. Similarly, SiO_2 was chosen as the dielectric substrate due to its non-lossy characteristics at optical wavelengths and its significant negative permittivity across the entire optical spectrum, rather than having a large imaginary component. These attributes of SiO_2 facilitate effective impedance matching and result in a broader and more comprehensive absorption bandwidth [42]. SiO_2 assists the suggested structure effectively maintains coupling the capacitance and the inductance, resulting within the expansion of the bandwidth with maximum absorbance suitable for solar cells application. Furthermore, it is worth noting that both nickel (Ni) and silicon dioxide (SiO_2) possess elevated melting points, ensuring exceptional thermal stability of the structure. In this particular case, the y-axis was selected as the position for the perfect magnetic boundary condition that occurs on a regular basis, and the perfect electric periodic boundary condition was x-axis. Once the operating optical frequency has incident parallel to the + z direction on the MMA's top layer, the waveguide port is able for flow through the interior structure of it. To reduce scattering, a layer which matches perfectly for open space is employed in conjunction with the z-axis. A linearly polarized planar wide-spectrum wave strikes the upper surface of the absorber. Both TE and TM modes, a floquet port was configured along the z-axis, using an x-axis master as well as a y-axis slave. The electric field and magnetic field are, respectively, asymmetrical for a conductor which is perfect-electric (PE) and symmetrical for material is considered a conductor which is perfectly magnetic (PM) with mutually orthogonal x, y, and z planes.

Design of the structure

A wide bandwidth of strong absorption is required crucial for maintaining physical measurements of the back layer, dielectric, and resonator. Figure 1a–e represents the proposed unit cell progression development technique and on the other hand dimensions are seeable in Fig. 1f–g where nickel is seeable in green and SiO_2 in off-white. Here,

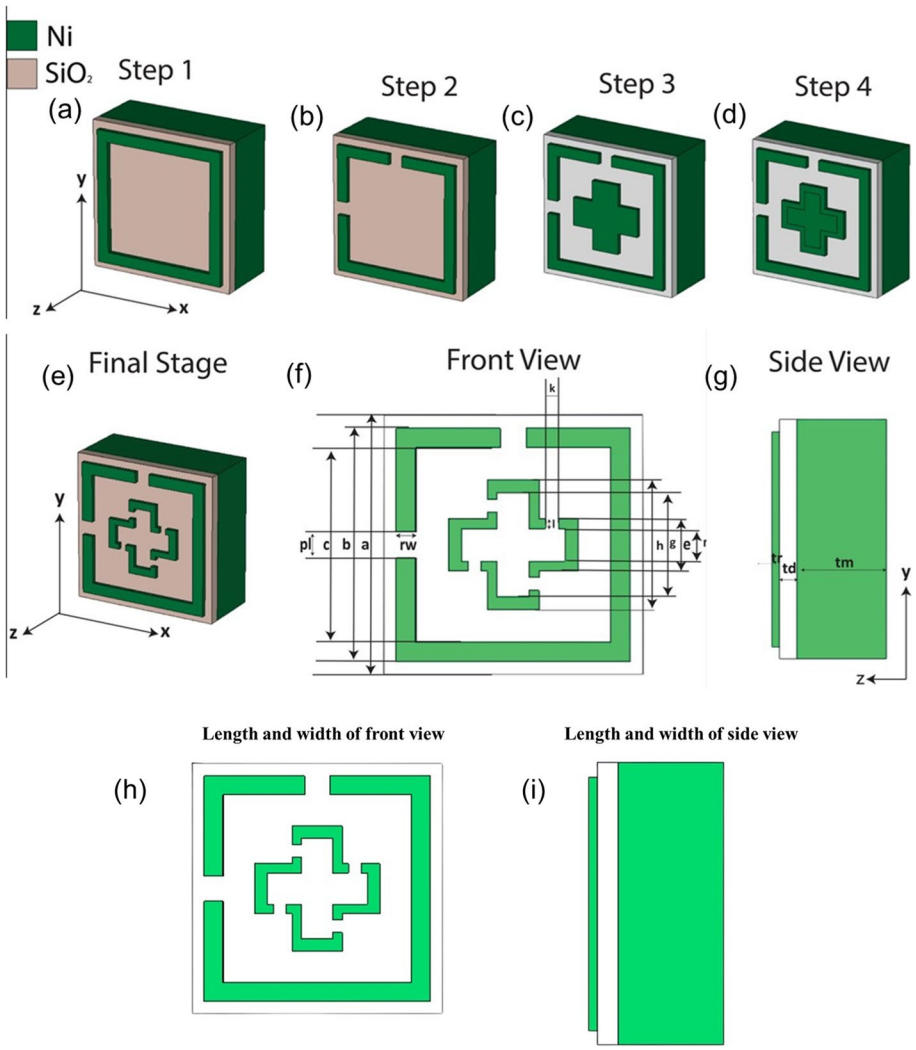

Fig. 1 Assessment regarding the designed unit cell structure: **a** step 1—incorporating the ground layer, **b** step 2—introduction of the dielectric layer, **c** step 3—addition of a single square box along with a plus, **d** step 4—incorporating one square box with two plus signs, **e** step 5—utilizing one square box and a plus sign, **f** step 6—final design with cutting portion details, **g** the concluding stage featuring slip gaps, **h** the length and width of unit cell design in front view along the y–z axis, and **i** the length and width of side view along the y–z axis

nickel (Ni) and silicon dioxide (SiO_2) are used to create a three-layered sandwich the structure features SSR stands for symmetrical shape resonator, rendering the style polarization-insensitive also nullifying the polarization conversion ratio (PCR). The ultimate style is selected for its outstanding qualities of absorption, as detailed in the "Methodology" section. We begin the design process in this phase by incorporating the back layer and dielectric layer, which have a combined length and width of a = 400 nm.

Following that, in Fig. 1a, a square box with dimensions b and c of 360 nm and 300 nm, respectively, is introduced. The layer specifications in Fig. 1g are as follows: the thickness of the back layer (tm) is 150 nm, the thickness of the dielectric layer (td) is 30 nm, and the thickness of the upper layer (tr) is 14 nm. Moving on to the second step, shown in Fig. 1b, a square box cutout with dimensions pl = 40 nm and rw = 80 nm is performed.

Following that, in the third step, two symmetrical shapes with dimensions h = 200 nm and e = 80 nm are combined to form a plus shape, as shown in Fig. 1c. The fourth step, depicted in Fig. 1d, introduces another plus shape with dimensions g = 160 nm and r = 50 nm. This shape is then refined further to form a plus shape configuration. Following that, the plus shape is cut with dimensions k = 20 nm and l = 30 nm, resulting in the final design shown in Fig. 1e. It is worth noting that the overall thickness of the unit cell design is 194 nm, indicating that it is an ultrathin structure. Nickel (Ni) is depicted in green in the visual representation, while silicon dioxide (SiO_2) is depicted in an off-white color.

Results and discussion

Methodology

Two key factors, transmittance (T) and reflectance (R), form a clear theoretical framework for the creation of the ideal metamaterial absorber. The Nicolson-Ross-Weir (NRW) equation was utilized; we calculated the absorptive characteristics of the envisaged configuration [43].

$$A(\omega) = 1 - R(\omega) - T(\omega) = 1 - |S_{11}(\omega)|^2 - |S_{21}(\omega)|^2 \tag{1}$$

Here, $R(\omega) = |S_{11}(\omega)|^2$ is the reflection, and $T(\omega) = |S_{21}(\omega)|^2$ is the transmission. To obtain maximum absorption, $S_{11}(\omega)$ and $S_{21}(\omega)$ ought to be maintained at a minimum level. Negligible transmission can be obtained by utilizing a metallic plate with an electromagnetic skin depth sufficient to prevent light-wave permeation. The suggested model employs nickel (Ni) as a ground to block light, with $S_{21} = 0$ [44]. So, we can write Eq. (1) as:

$$A(\omega) = 1 - |S_{11}(\omega)|^2 \tag{2}$$

The "coupled system" method, as it is also known, has been used in the current investigation. In this implementation, the suggested metamaterial perfect absorber (MPA)'s proposed skin depth is exceeded by the ground plane's lossy nickel material, which operates in the visible frequency band [31].

The reflection coefficient $S_{11}(\omega)$ under normal incidence can be computed using Eq. (3) as [45]:

$$S_{11}(\omega) = [Z(\omega) - Zo]/[Z(\omega) + Zo] \tag{3}$$

Here, $Z(\omega)$ denotes the input impedance of the metamaterial absorber, as well as Zo represents the impedance of free space, which is typically expressed as 120π or 376.76Ω. To attain complete reflection cancelation, it is necessary for the impedance $Z(\omega)$ of the metamaterial absorber to match the free space impedance Zo. The impedance of the ratio of permittivity εr determines the value entered into $Z(\omega)$ and relative permeability μr values. As a result, $Z(\omega)$ can be expressed as follows [46]. The absorption properties are determined by the structure's impedance matching. Equation was used to calculate the relative impedance (Z) of the recommended sandwich design with three separate sections (Eq. 4) [47]. The nearly perfect genuine value portion and the nearly

insignificant unreal part's value indicate that the structure's reflecting impedance perfectly matches the impedance of empty space, resulting in high absorption.

$$Z = \sqrt{(1+S11)^2 - \frac{S21^2}{(1-S11)^2} - S21^2} = \sqrt{\mu/\varepsilon}/Z_0 = \sqrt{\mu/\varepsilon r} \tag{4}$$

There is a strong near-field interaction between the ground plane and the array of nickel-based resonators. When considering this coupling effect, the theoretical findings from interference models closely match the outcomes of numerical simulations. The goal of this system's working principle, which is linked to destructive interference in reflection, in order to achieve impedance alignment with open space. Additionally, because of the ground plane, there is zero transmission. The geometrically structured surface, meticulously distributed with charges caused by magnetic and electric fields, constitutes the next influential element contributing to perfect absorption.

Characteristics of absorption

Figure 2a illustrates the design's absorption properties for different modes, especially TE and TM, throughout a wavelength range of 350–1500 nm. The absorption levels exhibit excellence in this spectral range, which covers the ultraviolet to the near-infrared domain, with a precisely adjusted mean absorption of 96.27%. Here, we found that the resonant wavelength is observed to be 694.89 nm with absorption 99.99% which is close to unity. This paper only focuses on the zone from 390 to 780 nm wavelength and this range is suitable for optical region. In this range, we get an average absorption of 97.17% and more importantly the absorption level consistently remains above 92%. All of this done by analyzing the data. There is no doubt that the proposed unit cell process wideband absorption and it covers for all optical wavelengths application and make it a suitable for solar energy harvesting technology. In Fig. 2b, we see the process of steps of the designs range from 390 to 780 nm and best absorption is selected last. The models shown in Fig. 1c through f, which correspond to steps 3 through 6, are shown in a progression in Fig. 1. The last stage is represented by the simulation design shown in Fig. 1i. None of the designs, with the exception of those shown in Fig. 1c and g, achieves

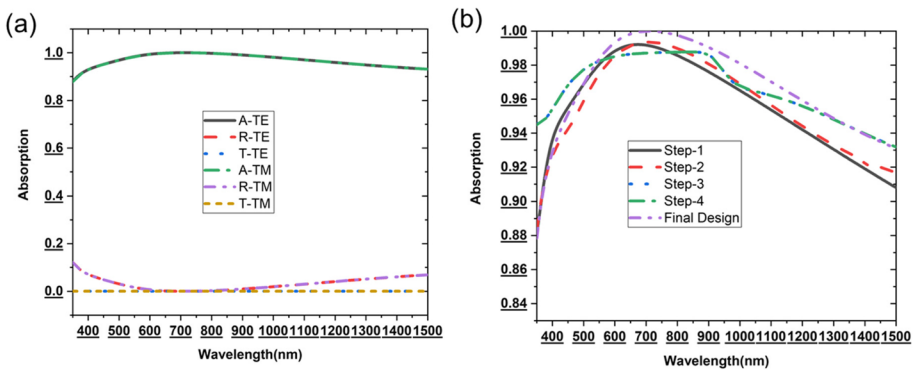

Fig. 2 **a** Plot displaying absorption, reflection, and transmission characteristics across the wavelength range of 350–1500 nm, **b** comprehensive assessment of the design progression from step 1 to the finalized design

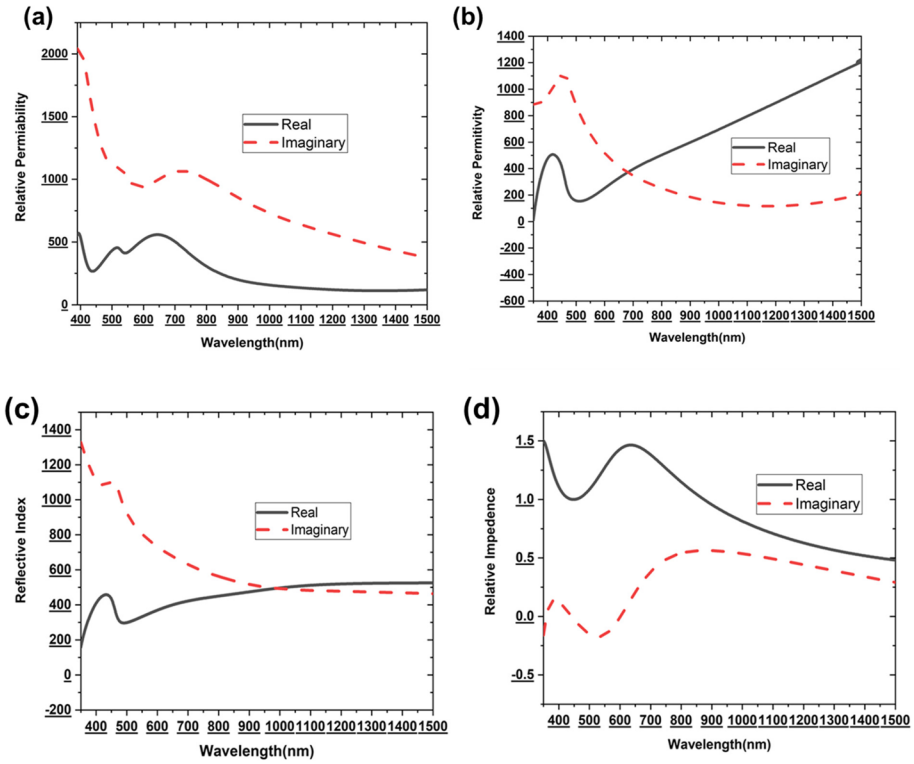

Fig. 3 **a** Graph depicting the relationship between relative permeability and wavelength for the NMA, **b** changing relative permittivity with respect to wavelength for the NMA, **c** refractive index as a function of wavelength for the NMA, and **d** relative impedance across various wavelengths for the NMA

near-unity absorbance. A wide-band absorbance that is close to unity, as seen in the finalized design in Fig. 1g, especially highlights the device's excellent efficiency.

Derivation of metamaterial characteristics for the NMA

The electromagnetic qualities of a NMA are completely dependent on elements such as resonator pattern, dimensional qualities, materials used, and associated parameters. The electromagnetic properties of the proposed NMA can be extracted and determined using the Nicolson-Ross-Weir equation [43], which includes factor parameters like the refractive index (RI), relative permeability, along with relative permittivity revealed in Fig. 3a to d. In this regard, it is significant to note that, as shown clearly in Fig. 3a, actual component of relative permeability for the proposed NMA demonstrates a positive value within the higher wavelength region covered by the desired wavelength range. Additionally, as seen in Fig. 3b, the suggested NMA real component of relative permittivity assumes a good value within the visible wavelength domain. Additionally, Fig. 3c shows that within certain regions of the higher visible wavelength range, the real component of the refractive index takes on a negative value. Figure 3d makes it clear that there is a noticeable increase in the level of absorption as the real component of impedance approaches unity and the imaginary components tend towards zero. As a result, the suggested NMA design displays unique metamaterial properties, including positive permeability as well as a low refractive index.

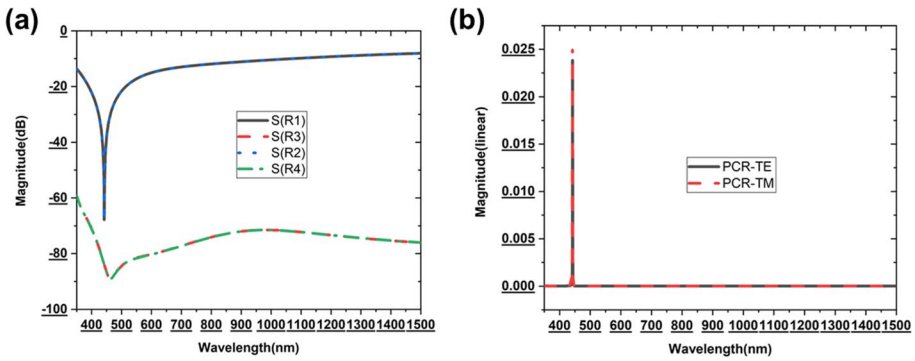

Fig. 4 Illustrations of **a** S-parameters both for TE and TM modes and **b** PCR both for TE and TM modes, respectively

S-polarization and P-polarization with the calculated polarization conversion ratio (PCR)

It belongs to a well-established principle that a NMA should primarily absorb electromagnetic (EM) waves rather than converting them. While the proposed model demonstrates excellent symmetry, as previously substantiated, it is essential to confirm that the particular cell as created fails alter the EM polarization. This verification is achieved by analyzing the s- and p-polarization components, as defined by Eqs. (5) and (6) and highlighted in Fig. 4a. In Fig. 4a, the p-polarization component closely approaches a magnitude of zero in decibels (dB), signifying that the structural geometry does not alter the characteristics of the incident EM waves.

$$|S_{11}(\omega)|^2 = |S_{E,E}(\omega)|^2 + |S_{E,M}(\omega)|^2 = R1^2 + R2^2 \tag{5}$$

$$|S_{11}(\omega)|^2 = |S_{M,M}(\omega)|^2 + |S_{M,E}(\omega)|^2 = R3^2 + R4^2 \tag{6}$$

Here, $|S_{E,\,E}\,(\omega)|^2 = |S_{M,\,M}\,(\omega)|2 = R1^2 = R3^2 =$ s-polarization component alongside $|S_{E,\,M}\,(\omega)|^2 = |S_{M,\,E}\,(\omega)|2 = R2^2 = R4^2 =$ p-polarization component.

$$PCR_E = R2^2/(R1^2 + R2^2) \tag{7}$$

$$PCR_M = R4^2/(R3^2 + R4^2) \tag{8}$$

Furthermore, in Eqs. (6) and (7), the PCR is computed, according to Fig. 4b. The fact is obvious that the PCR values for both TE and TM polarizations are nearly zero, indicating the absence PCR characteristics in the NMA.

Polarization insensitivity and stability under oblique incident angles

The recommended polarization insensitivity metamaterial absorber (MMA) was extensively studied to validate its absorption effectiveness. In the TE mode, the z-axis corresponds to the wave propagation guidance, with the magnitude of the field vector (Hz) aligned with the z-axis. Additionally, the electric field vector (Ex) and magnetic field vector (Hy) are orientated with the x- and y-axes, respectively.

Conversely, in the TM mode, the electric field vector (Ez) aligns with the propagation guidance of waves while the magnetic (Hz) and electric (Ey) field vectors align with the x and y axes, respectively. Notably, because to its intrinsic axial and rotational symmetry, the proposed MMA exhibits remarkable absorption capabilities throughout a wide range of polarization incidence angles (ϕ) up to 90°. It is important to note that all the aforementioned conclusions were generated from simulations assuming a normal incident angle (θ = 0°). However, practical applications generally entail electromagnetic (EM) waves entering at an oblique incidence angle relative to the MMA structure. Therefore, the analysis of absorption behavior for oblique incident angles (θ) is equally significant. Figure 5a and b illustrate the absorption curves for both TE and TM modes at oblique incidence angles (θ) ranging from 60 to 70°, respectively.

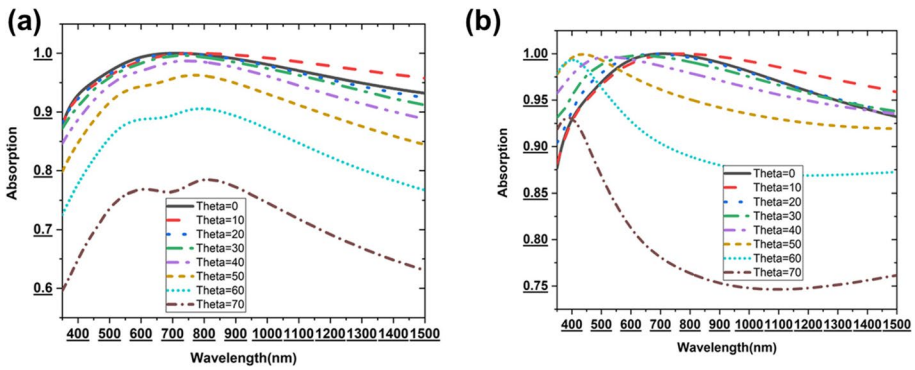

Fig. 5 **a** TE mode for oblique incidence angles (θ) from 0 to 70°, **b** TM mode for oblique incidence angles (θ) from 0 to 70°

Table 1 List of the proposed unit cell's parameters

Parameters	a	b	c	h	g	e	rw	k	r	l	tm	tr	td	pl
Values (nm)	400	360	300	200	160	80	80	20	50	30	150	14	30	40

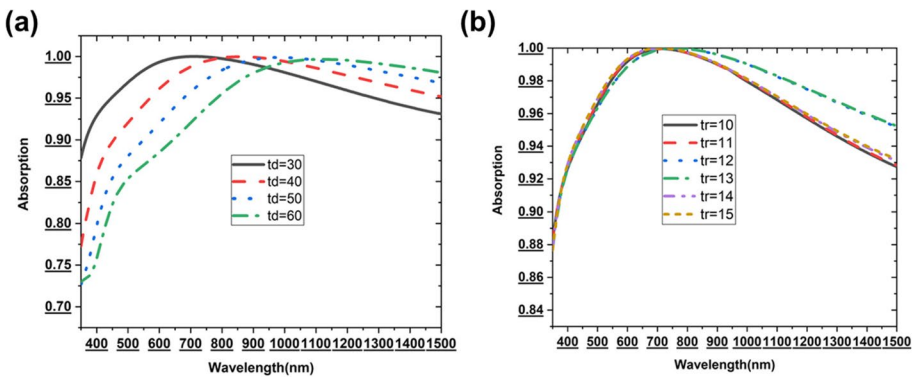

Fig. 6 **a** Substrate thickness td and **b** upper layer thickness tr

Geometric parameter sweep

According to Table 1, our "Methodology" section analysis focuses primarily on two essential parameters, namely "tr" and "td." The "ts" parameter, which represents the thickness of the front-layer metal, has a significant influencing absorption characteristic of our suggested structure, as shown in Fig. 6a. The "tr" parameter is systematically adjusted from 10 to 15 nm in 1-nm increments in this investigation. Surprisingly, when "tr" = 14 nm, the average absorption peaks. Furthermore, when the width of each segment of the metal resonator grows, we see a red-shift phenomenon within the absorption band. This behavior can be explained by the increased total equivalent permittivity associated with the metamaterial's rising thickness. Since the outcome of this, both the resonance wavelength and the absorption band redshift, in accordance with the concept of the equivalent medium [48] and the λ/4 resonance model [49]. Figure 6b also shows the effect of altering the dielectric thickness parameter "td," which ranges from 30 to 60 nm with a 10-nm increment. Notably, when "td" is set to 30 nm, the structure reaches its maximum mean absorption. As with the "tr" parameter, increasing "td" causes a red shift in the peak absorption. The inverse connection within the region among the ground layer and the resonator, there is a correlation between dielectric strength and capacitance, causes this behavior. As "td" expands, the capacitance reduces, changing the impedance matching and causing the red shifting shown in the MMA layout. Variations within the variable dielectric dimension "td" and the resonator dimension parameter "tr" can be used to create resonances at different wavelengths, resulting in a considerable spectrum gap, which holds promise for sensing applications. Because of its spectral tweaking capabilities, the suggested structure is appropriate for a wide range of sensing applications.

Comparative analysis of absorption phenomenon using different metals and dielectric layers

The absorbance properties of several metals and dielectric materials are demonstrated in Fig. 7a. SiO_2, a dielectric substance, and nickel, a metal, both show a significantly high average absorption; however, it is crucial to note that different metal and dielectric combinations have the potential to serve in a variety of optical applications. GaAs, Si_3N_4, AiN, amorphous Si, and SiO_2 are among the dielectric

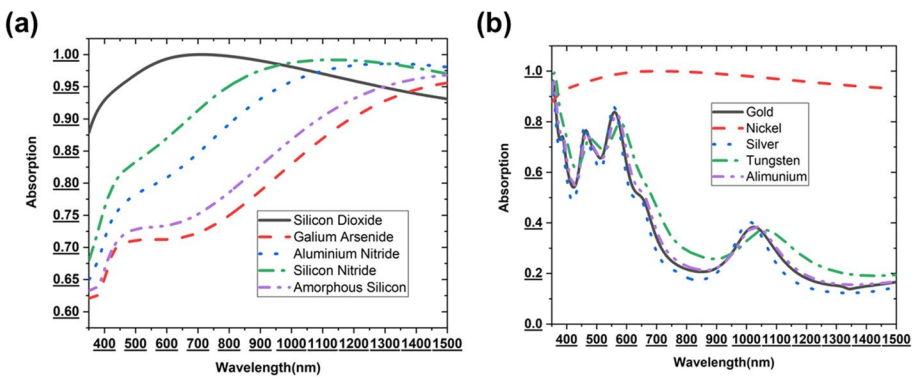

Fig. 7 **a** Dielectric substrates and **b** metal

materials compared in this inquiry. SiO_2 becomes an effective absorber when the insulator film's refractive index drops, and thus lead it to be the material of choice within the absorber layout suggested. The suggested model's absorption characteristics for several metals, notably nickel, tungsten, silver, copper, and gold, are depicted in Fig. 7b. Because of its good impedance matching within the suggested unit cell, especially within the visible also near-infrared spectrum, nickel demonstrates the maximum absorption.

Mechanism of absorption with electric field and magnetic field

Here, we mainly seen the electric field and magnetic field of the absorber for the peck and minimum absorption frequency of 694.89 nm and 456.88 nm, respectively, shown in Figs. 8 and 9. In Fig. 8, we mainly seen the electric field for two modes and they are TE and TM both are highlighted for peck and low absorption. Here, in the peck absorption, we seen that the absorption high both for TE and TM modes in Fig. 8a and b but for low absorption TE and TM indicates low amount of absorption that are seen in Fig. 8c and d. Again, for magnetic field, the peck absorption was seen in Fig. 9a and b both for TE and TM modes.

But we saw the low absorption for magnetic field in Fig. 9c and d both for TE and TM modes.

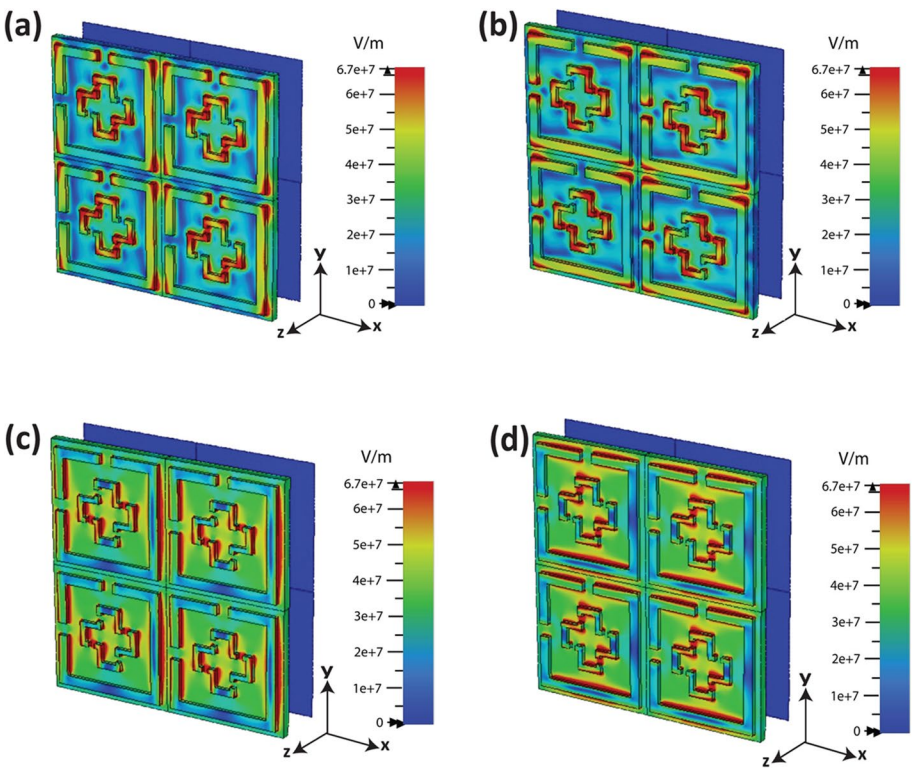

Fig. 8 E-field peck absorption at **a** TE—694.89 nm, **b** TM—694.89 nm. Again, low absorption at **c** TE—456.88 nm and **d** TM—456.88 nm

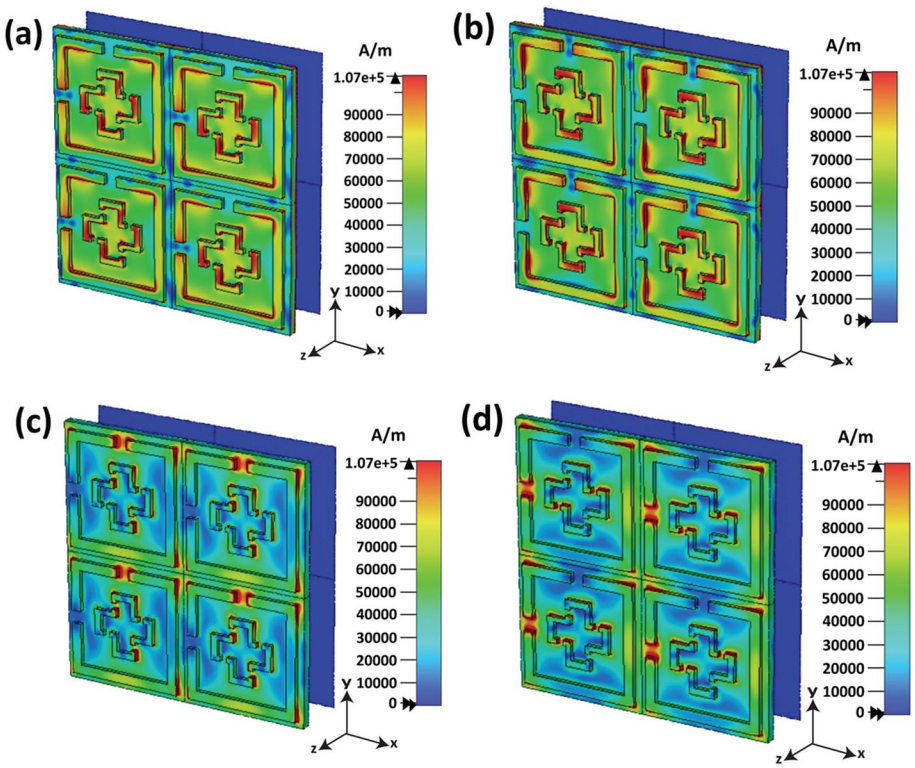

Fig. 9 H-field peck absorption at **a** TE—694.89 nm, **b** TM—694.89 nm. Again, low absorption at **c** TE—456.88 nm and **d** TM—456.88 nm

Comparative study

Table 2 shows a comparison of the suggested MMA with recent research carried out in the same wavelength range. The suggested design has an exceptionally high average absorption of 97.17% and a peak absorption of 99.99%. The suggested design displays 70° of angular stability, sustaining over 70% absorbing capacity within the defined range, which is superior to conventional broadband absorbers. As a result, the suggested NMA has the potential to be utilized in energy-harvesting technology. The proposed model separates from other comparable models in that it uses high-temperature-resistant materials, like nickel and SiO_2, to offer thermal stability and prevent overheating. Furthermore, the use of nickel as a ground layer reduces the need for quartz in the base structures, resulting in cost savings. The suggested structure stands out compared to other similar NMAs due to its versatility and features such as inexpensive material prices, wide-angle stability, polarization independence, structural compactness, thermal stability, and favorable mean absorption rates within the visible regime.

Conclusions

In summary, this study investigates the radiative properties of a nickel and SiO_2-based ultrathin (194 nm), mechanically flexible, wide-angle incident, and polarization-insensitive metamaterial absorber (NMA). Nickel is used as the metallic component,

Table 2 Comparison of different reported NMAs with the proposed absorber

Range (nm)	Dimensions (nm)	Layer	Materials	Polarization-insensitive	Angular stability for up to 70% absorption	Absorption level at 0°	Peak absorption at 0°	Average absorption	Validation	Ref
490–825	250 × 250 × 344	Three	Ag, Al_2O_3	Yes	$\theta \leq 60°$	Above 90%	99%	N/A	Simulated	[50]
400–700	250 × 250 × 355	Three	Ni, Si	Yes	60°	N/A	99%	90%	Simulate and measured	[51]
389–700	400 × 400 × 99	Three	W, SiO_2	Yes	$\theta \leq 30°$	Above 85%	99%	92.2%	Simulated	[52]
400–800	300 × 300 × 250	Three	W, SiO_2	Yes	$\theta \leq 70°$	Above 90%	99.3%	98%	Simulated	[53]
380–760	240 × 240 × 170	Two	Au, Si	Yes	N/A	Above 90%	99.1%	93.9%	Simulated	[54]
450–600	400 × 400 × 115	Three	Al, SiO_2	No	N/A	Above 50%	99%	95%	Simulated	[55]
389–697	1000 × 1000 × 225	Three	W, SiO_2	Yes	$\theta \leq 60°$	Above 91.24%	99.9%	96.77%	Simulated and calculated	[56]
380–760	300 × 300 × 75	Two	TiN, TiO_2	Yes	$\theta \leq 40°$	Above 91%	97%	94%	Simulated	[57]
375–750	1000 × 1000 × 165	Three	W, quartz	Yes	$\theta \leq 45°$	Above 66.66%	99.92%	90%	Simulated	[58]
460–772	1000 × 1000 × 174	Three	Al, SiO_2	No	N/A	Above 40%	93%	60%	Simulated	[59]
300–680	1555 × 1555 × 560	Three	A-Si, Ag, ITO	Yes	$\theta \leq 50°$	Above 90%	99%	90.10%	Simulated	[60]
460–670	1000 × 1000 × 644	Three	Au, SiO_2	Yes	$\theta \leq 80°$	Above 40%	99.9%	N/A	Simulated and measured	[61]
400–700	N/A	Three	Cu, Si_3N_4, Si	No	N/A	80%	97%	N/A	Simulated and measured	[62]
390–780	400 × 400 × 194	Three	Ni and SiO_2	Yes	$\theta \leq 70°$	Above 92.22%	99.99%	97.17%	Simulated and calculated	Proposed

providing an excellent impedance match, and is combined with the SiO_2 dielectric with a low refractive index in a sandwiched metal-dielectric-metal setup. Based on the results of our numerical calculations, the proposed NMA has an average broadband absorption spectrum of 97.17% within the wavelength range of 390–780 nm and a minimum absorption rate of 92.22%. Furthermore, the model's capability allows it to be used to the UV, optical, and NI spectral areas, where it achieves an outstanding mean rate of absorption greater than 96.27% spanning the wavelength range of 350 to 1500 nm. This design is ideal for a variety of applications, including solar energy harvesting and solar-thermal photovoltaic (STPV) systems. Furthermore, the shift in resonance wavelength offers up possibilities for using the device as a solar sensor or refractive index sensor. Furthermore, the linear increase in absorbance when the dielectric layer transitions to Si_3N_4 highlights its potential as a light detector. This design's combination of mechanical flexibility and temperature stability, together with its symmetrical shape, makes it an excellent pick for a variety of demands throughout the visible-wavelength range.

Acknowledgements
The author received no external funding/support.

Authors' contributions
I.M.T.I. (Istiaq Mohammad Tanvirul Islam) made significant contributions to this study regarding conception, design, and analysis and writing the manuscript. S.S.I. (Sikder Sunbeam Islam), M.R.I. (Md. Rashedul Islam), R.I. (Rezaul Azim), and A.N.M.R. (Abu Naser Md. Rezaul) participated in the revision of the article for important intellectual content. All authors have read and approved the manuscript.

Funding
The author(s) received no financial support for the research.

Availability of data and materials
The data can be shared upon request by contacting the corresponding author.

Declarations

Competing interests
The authors declare no competing interests.

Received: 29 December 2023 Accepted: 4 June 2024
Published online: 14 June 2024

References

1. Rufangura P, Sabah C (2017) Graphene-based wideband metamaterial absorber for solar cells application. J Nanophotonics 11(3):036008–036008
2. Veselago VG (1968) The electrodynamics of substances with simultaneously negative values of img align= absmiddle Alt= ϵ Eps/Img and μ. Phys Usp 10(4):509–514
3. Walser RM (2001) Electromagnetic metamaterials. In: Complex mediums II: beyond linear isotropic dielectrics, vol. 4467:1–15. SPIE.
4. Chen C, Lei J, Liu Z (2022) A ternary seismic metamaterial for low frequency vibration attenuation. Materials 15(3):1246
5. Sinha K, Islam SS, Hossain MJ (2020) A combined WU-shaped NRI metamaterial for dual band microwave application. Univ J Electr Electron Eng 7(2):81–87
6. Afsar MSU, Faruque MRI, Hossain MB (2022) Holy cross-moon shaped dual band perfect metamaterial absorber for C-band application. Mater Today Commun 33:104309
7. Landy NI, Sajuyigbe S, Mock JJ, Smith DR, Padilla WJ (2008) Perfect metamaterial absorber. Phys Rev Lett 100(20):207402
8. Chu P, Chen J, Xiong Z, Yi Z (2020) Controllable frequency conversion in the coupled time-modulated cavities with phase delay. Optics Commun 476:126338
9. Cai R, Rao W, Zhang Z, Long F, Yin Y (2014) An imprinted electrochemical sensor for bisphenol A determination based on electrodeposition of a graphene and Ag nanoparticle modified carbon electrode. Anal Methods 6(5):1590–1597
10. Li-Ying J et al (2021) A four-band perfect absorber based on high quality factor and high figure of merit of monolayer molybdenum disulfide.

11. Cheng Y et al (2020) Strongly enhanced local electromagnetic field in mid-infrared and terahertz photodetectors employing a hybrid antenna. AIP Adv 10(1).
12. Islam SS, Chowdhury A, Paul N, Ahmed S (2018) Electromagnetic absorption comparison of dipole and microstrip patch antenna in the human head. In: 2018 9th IEEE annual ubiquitous computing, electronics & mobile communication conference (UEMCON). 1038–1041: IEEE.
13. Islam SS, Faruque MRI, Islam MT (2016) A new NZRI metamaterial for electromagnetic cloaking operation. Int J Appl Electromagnet Mech 50(1):145–153
14. Zhang L et al (2022) Multifunctional nanotheranostics for near infrared optical imaging-guided treatment of brain tumors. Adv Drug Deliv Rev 190:114536
15. Bilal R et al (2020) Elliptical metallic rings-shaped fractal metamaterial absorber in the visible regime. Sci Rep 10(1):14035
16. Rana AS, Zubair M, Anwar MS, Saleem M, Mehmood MQ (2020) Engineering the absorption spectra of thin film multilayer absorbers for enhanced color purity in CMY color filters. Optic Mater Express 10(2):268–281
17. Altıntaş O, Aksoy M, Ünal E (2020) Design of a metamaterial inspired omega shaped resonator based sensor for industrial implementations. Physica E 116:113734
18. Vora A, Gwamuri J, Pala N, Kulkarni A, Pearce JM, Güney DÖ (2014) Exchanging ohmic losses in metamaterial absorbers with useful optical absorption for photovoltaics. Sci Rep 4(1):4901
19. Liu S, Yin X, Zhao H (2022) The tunable single-/narrow-band terahertz metamaterial absorber through photoconductivity. Res Phys 39:105741
20. Chowdhury IH, Mazumder MMR, Islam SS, Islam MT, Soliman MS, Islam MS (2024) Ultrawideband nanostructured metamaterial absorber with an octagon-packed star-shaped resonator for UV to NIR spectrum wavelength application. Ain Shams Eng J. 102653.
21. Ahamed E, Hasan MM, Faruque MRI, Mansor MFB, Abdullah S, Islam MT (2018) Left-handed metamaterial inspired by joint TD geometry on flexible NiAl2O4 substrate. PLoS ONE 13(6):e0199150
22. Hossain MJ, Faruque MRI, Islam MT (2018) Effective medium ratio obeying wideband left-handed miniaturized meta-atoms for multi-band applications. J Electron Mater 47:1859–1870
23. Wang Y, Xuan X-F, Zhu L, Yu H-J, Gao Q, Ge X-L (2021) Numerical study of an ultra-broadband, wide-angle, polarization-insensitive absorber in visible and infrared region. Opt Mater 114:110902
24. Zhang T et al (2021) Recent progress on nanostructure-based broadband absorbers and their solar energy thermal utilization. Front Chem Sci Eng 15:35–48
25. Huang X, Yang H, Yu S, Wang J, Li M, Ye Q (2013) Triple-band polarization-insensitive wide-angle ultra-thin planar spiral metamaterial absorber. J Appl Phys 113(21).
26. Shrekenhamer D, Watts CM, Montoya J, Krishna S, Padilla WJ (2013) Metamaterial-based imaging for potential security applications. In: Photonic and phononic properties of engineered nanostructures III. 8632:195–201. SPIE.
27. Wang B-X, Zhai X, Wang G, Huang W, Wang L (2014) Design of a four-band and polarization-insensitive terahertz metamaterial absorber. IEEE Photonics J 7(1):1–8
28. Pan H, Zhang H (2021) Thermally tunable polarization-insensitive ultra-broadband terahertz metamaterial absorber based on the coupled toroidal dipole modes. Opt Express 29(12):18081–18094
29. Tang J, Xiao Z, Xu K, Liu D (2016) A polarization insensitive and broadband metamaterial absorber based on three-dimensional structure. Optics Commun 372:64–70
30 Islam MT, Samsuzzaman M, Islam MT, Kibria S, Singh MJ (2018) A homogeneous breast phantom measurement system with an improved modified microwave imaging antenna sensor. Sensors 18(9):2962
31. Tao H, Landy NI, Bingham CM, Zhang X, Averitt RD, Padilla WJ (2008) A metamaterial absorber for the terahertz regime: design, fabrication and characterization. Opt Express 16(10):7181–7188
32. Zhang Z, Yu Z, Liang Y, Xu T (2018) Dual-band nearly perfect absorber at visible frequencies. Optical Materials Express 8(2):463–468
33. Zhou Y, Luo M, Shen S, Zhang H, Pu D, Chen L (2018) Cost-effective near-perfect absorber at visible frequency based on homogenous meta-surface nickel with two-dimension cylinder array. Opt Express 26(21):27482–27491
34. Ünal E, Bağmancı M, Karaaslan M, Akgol O, Sabah C (2018) Strong absorption of solar energy by using wide band metamaterial absorber designed with plus-shaped resonators. Int J Mod Phys B 32(25):1850275
35. Hoque A, Islam MT (2020) Numerical analysis of single negative broadband metamaterial absorber based on tri thin layer material in visible spectrum for solar cell energy harvesting. Plasmonics 15(4):1061–1069
36. Hakim ML et al (2022) Wide-oblique-incident-angle stable polarization-insensitive ultra-wideband metamaterial perfect absorber for visible optical wavelength applications. Materials 15(6):2201
37. Zhu W et al (2017) Wideband visible-light absorption in an ultrathin silicon nanostructure. Opt Express 25(5):5781–5786
38. Heidari M, Sedighy S (2018) Broadband wide-angle polarization-insensitive metasurface solar absorber. JOSA a 35(4):522–525
39. Katrodiya D, Jani C, Sorathiya V, Patel SK (2019) Metasurface based broadband solar absorber. Opt Mater 89:34–41
40. Ghosh G (1999) Dispersion-equation coefficients for the refractive index and birefringence of calcite and quartz crystals. Optics Commun 163(1–3):95–102
41. Bagmanci M, Karaaslan M, Unal E, Akgol O, Bakır M, Sabah C (2019) Solar energy harvesting with ultra-broadband metamaterial absorber. Int J Mod Phys B 33(08):1950056
42. Kanmaz I, Abdullah Ü (2021) Silicon dioxide thin films prepared by spin coating for the application of solar cells. Int Adv Res Eng J 5(1):14–18
43. Hossain MJ, Faruque MRI, Ahmed MR, Alam MJ, Islam MT (2019) Polarization-insensitive infrared-visible perfect metamaterial absorber and permittivity sensor. Res Phys 14:102429
44. Shuvo MMK, Hossain MI, Rahman S, Mahmud S, Islam SS, Islam MT (2021) A wide-angle, enhanced oblique incidence, bend-able metamaterial absorber employed in visible region with a sun shape resonator. IEEE Access 9:126466–126480

45. Smith D, Vier D, Koschny T, Soukoulis C (2005) Electromagnetic parameter retrieval from inhomogeneous metamaterials. Phys Rev E 71(3):036617
46. Ziolkowski RW, Heyman E (2001) Wave propagation in media having negative permittivity and permeability. Phys Rev E 64(5):056625
47. Cen C et al (2020) High quality factor, high sensitivity metamaterial graphene—perfect absorber based on critical coupling theory and impedance matching. Nanomaterials 10(1):95
48. Smith DR, Pendry JB (2006) Homogenization of metamaterials by field averaging. JOSA B 23(3):391–403
49. Chen X et al (2018) An ultra-broadband and lightweight fishnet-like absorber in microwave region. J Phys D Appl Phys 51(28):285002
50. Zhang H-F, Liu H-B, Hu C-X, Wang Z-L (2020) A metamaterial absorber operating in the visible light band based on a cascade structure. Plasmonics 15:1755–1766
51. Luo M, Shen S, Zhou L, Wu S, Zhou Y, Chen L (2017) Broadband, wide-angle, and polarization-independent metamaterial absorber for the visible regime. Opt Express 25(14):16715–16724
52. Charola S, Patel SK, Dalsaniya K, Jadeja R, Nguyen TK, Dhasarathan V (2021) Numerical investigation of wideband L-shaped metasurface based solar absorber for visible and ultraviolet region. Physica B 601:412503
53. Rana AS, Mehmood MQ, Jeong H, Kim I, Rho J (2018) Tungsten-based ultrathin absorber for visible regime. Sci Rep 8(1):2443
54. Li C, Fan H, Dai Q, Wei Z, Lan S, Liu H (2019) Multipole resonance in arrays of diamond dielectric: a metamaterial perfect absorber in the visible regime. Nanomaterials 9(9):1222
55. Lai Y-C, Chen C-Y, Hung Y-T, Chen C-Y (2020) Extending absorption edge through the hybrid resonator-based absorber with wideband and near-perfect absorption in visible region. Materials 13(6):1470
56. Mahmud S, Islam SS, Mat K, Chowdhury ME, Rmili H, Islam MT (2020) Design and parametric analysis of a wide-angle polarization-insensitive metamaterial absorber with a star shape resonator for optical wavelength applications. Results Phys 18:103259
57. Zhong H et al (2020) Thermal-stability resonators for visible light full-spectrum perfect absorbers. Sol Energy 208:445–450
58. Hossain I, Samsuzzaman M, Moniruzzaman M, Bais BB, Singh MSJ, Islam MT (2021) Polarization-independent broadband optical regime metamaterial absorber for solar harvesting: a numerical approach. Chin J Phys 71:699–715
59. Fang J, Wang B (2021) Optical capture capability enhancement by right-angled triangular visible absorber. Phys Lett A 404:127404
60. Zhang Y et al (2021) Dual band visible metamaterial absorbers based on four identical ring patches. Physica E 127:114526
61. Xu H, Hu L, Lu Y, Xu J, Chen Y (2019) Dual-band metamaterial absorbers in the visible and near-infrared regions. The Journal of Physical Chemistry C 123(15):10028–10033
62. Zhu P, Jay Guo L (2012) High performance broadband absorber in the visible band by engineered dispersion and geometry of a metal-dielectric-metal stack. Appl Phys Lett 101(24).

Publisher's Note